

APPLICATION

3-D optical modeling of thin-film silicon solar cells on diffraction gratings

Olindo Isabella^{1*}, Serge Solntsev¹, Diego Caratelli² and Miro Zeman¹¹ PVMD/DIMES, Delft University of Technology, Mekelweg 4, 2628 Delft, CD, The Netherlands² IRCTR, Delft University of Technology, P.O. Box 5031, 2600 Delft, GA, The Netherlands

ABSTRACT

An effective rigorous 3-D optical modeling of thin-film silicon solar cells based on finite element method (FEM) is presented. The simulation of a flat single junction thin-film silicon solar cell on thick glass (i.e., *superstrate* configuration) is used to validate a commercial FEM-based package, the High Frequency Structure Simulator (HFSS). The results are compared with those of the reference software, Advanced Semiconductor Analysis (ASA) program, proving that the HFSS is capable of correctly handling glass as an incident material within very timely, short, and numerically stable calculations. By using the HFSS, we simulated single junction thin-film silicon solar cells on glass substrates textured with one-dimensional (1-D) and two-dimensional (2-D) trapezoid-shaped diffraction gratings. The correctness of the computed results, with respect to an actual device, is discussed, and the impact of different polarizations on spectral response and optical losses is examined. From the simulations carried out, optimal combinations for period and height in both 1-D and 2-D grating configurations can be indicated, leading to short-circuit current percentage increase with respect to a flat cell of, respectively, 25.46% and 32.53%. With very limited computer memory usage and computational time in the order of tens of minutes for a single simulation, we promote the usage of 3-D FEM as a rigorous and efficient way to simulate thin-film silicon solar cells. Copyright © 2012 John Wiley & Sons, Ltd.

KEYWORDS

diffraction gratings; optical modeling; finite element method; thin-film silicon solar cells; light scattering; 3-D Maxwell equations solver

*Correspondence

Isabella, Olindo, PVMD/DIMES, Delft University of Technology, Mekelweg 4, 2628, Delft CD, The Netherlands.

E-mail: Olindo.Isabella@gmail.com

1. INTRODUCTION

Thin-film silicon solar cell technology relies on light management to enhance light absorption in thin absorber layers resulting in an increased photocurrent [1]. Although the use of randomly textured morphologies is nowadays regarded as the standard approach to achieve efficient scattering inside a solar cell [2–4], scattering of light from diffraction gratings is an alternative way to increase the level of scattering [5,6]. The variation of the geometrical parameters of the gratings, such as the period (P), the height (h), the shape, and the duty cycle (D_C), which is the ratio between the highest segments of the gratings' profile over the entire period, can lead to an optimum that results in the maximal photocurrents.

Recently, several groups have carried out research on thin-film silicon solar cells deposited on transparent

superstrates (*pin* sequence) [7] and opaque substrates (*nip* sequence) [8] patterned with one-dimensional (1-D) or two-dimensional (2-D) diffraction gratings [9,10]. The reported results on solar cell performance indicate that diffraction gratings have a potential as an alternative texturization for light scattering, but to achieve and possibly overcome the photocurrent levels obtained with the best random textures, they have to be properly optimized [11,12]. It has become clear that the analysis and optimal design of thin-film silicon solar cells on diffraction gratings require the adoption of rigorous three-dimensional (3-D) optical models. The first reported simulation studies focused primarily on the optical effects of light incident onto gratings [13,14]. Afterwards, various optimized methods for numerically solving Maxwell's equations have been used to optically simulate complete devices [15–19].

In this contribution, we present an effective approach of a rigorous 3-D modeling based on the finite element method (FEM). The High Frequency Structure Simulator (HFSS) [20] has been employed to carry out the simulations. As an example, we show simulations and optimizations of amorphous silicon (a-Si:H) solar cells textured with 1-D and 2-D periodic gratings on glass (*pin*-sequenced solar cells). We demonstrate that, by using the boundary conditions properly, 3-D simulations can be performed in a matter of minutes or a few hours with a conventional personal computer. At the beginning, we give an overview of different numerical methods for solving electromagnetic wave equations that have been used in simulations of thin-film solar cells in previous publications on this topic. We point out why FEM is a very suitable method for modeling thin-film solar cell structures with realistic optical properties of layers and realistic morphologies of interfaces. Results of validation through the comparison of simulation results with those obtained using other models are presented. Furthermore, verification of results through the comparison of the simulated and the measured external quantum efficiency (EQE) of a realistic cell deposited on periodic grating are shown for an a-Si:H solar cell. The optical losses and the effect of the polarization related to 1-D gratings are analyzed. By varying the P and h of the gratings, we indicate the optimal combination for 1-D and 2-D gratings resulting in a short-circuit current percentage increase of 25.5% and 32.5%, respectively, in comparison to a flat cell. Finally, the performance analysis of the simulator is evaluated in terms of memory usage and computational time.

2. AN OVERVIEW OF RIGOROUS MODELING APPROACHES FOR ANALYSIS OF THIN-FILM SOLAR CELLS

The finite-difference time-domain (FDTD) method [21] has been commonly used to solve electromagnetic problems in thin-film optoelectronic devices [22]. A complete analysis over a wide wavelength range can be carried out by one simulation run because the method works in the time domain. The electric and magnetic field components in a volume of space are evolved in time until the desired transient or steady-state electromagnetic field behavior is fully evolved. In the simple case of single wavelength calculation, FDTD modeling does not require parameterized optical properties of materials. However, for more complex and realistic cases, wavelength-dependent complex refractive indexes of layers have to be represented by dielectric functions parameterized with Lorentz-like oscillators [23]. For semiconductor materials such as amorphous silicon, more than three oscillators have to be superimposed to mimic the wavelength behavior of the desired dielectric functions [24]. This leads to convergence problems in finding the solution or, at least, problems in long computational time if the calculation conditions are

not properly chosen. Such problems also affect other numerical calculation methods. Another difficulty when using FDTD for the analysis of thin-film photovoltaic devices is related to metal back contacts. If realistic optical properties of metals such as silver or aluminum are used in simulations, convergence problems may arise. For this reason, most of the recent commercial FDTD software has algorithms that prevent divergence in the calculation of a model that includes metals.

The finite integration technique (FIT) is a spatial discretization scheme to numerically solve electromagnetic field problems in the time domain. The basic idea of this approach is to apply Maxwell's equations in integral form to a set of staggered grids [16]. This method stands out because of the high flexibility in geometric modeling and boundary handling, as well as the incorporation of arbitrary material distributions and material properties such as anisotropy, nonlinearity, and wavelength dependency. The use of a consistent dual orthogonal grid in conjunction with an explicit time integration scheme leads to memory-efficient algorithms. Successful use of FIT in simulations of thin-film silicon solar cells can be found in recent publication [25].

The rigorous coupled-wave analysis is an accurate computational method for the evaluation of electromagnetic modes in periodic dielectric configurations [17]. Maxwell's equations, arranged in partial differential form, as well as the boundary conditions, are expanded in terms of Floquet functions and turned into infinitely large algebraic equations. Depending on the accuracy and convergence speed needed, such a system can be made finite and, thus, solvable numerically through properly filtering out higher order Floquet functions. The rigorous coupled-wave analysis has been efficiently applied in simulations of thin-film silicon solar cells with periodically textured interfaces [26,27].

Another approach in solving partial differential equations, such as Maxwell equations, is the method of moments (MoM) [18]. In this method, calculations are executed only at the designed surface, rather than throughout the volume of space contained in it. For this reason, MoM is more efficient than the other approaches for small surface-to-volume ratio problems. The boundary element formulations and the treatment of fields only in linear homogeneous media are among the disadvantages of this approach, which lead, respectively, to computational time growing with the square of the problem size and to considerable restrictions to the range of problems solvable with this method. Usage of MoM in electromagnetic problems related to photovoltaics has been recently reported [28].

2.1. Finite element method

The FEM is a numerical technique used in finding approximate solutions of Maxwell equations. The volume of the simulated structure is meshed (i.e., discretized), with tetrahedrons and the electromagnetic field components

computed at their vertex (nodes). In this method, the Faraday and Ampere–Maxwell laws of the frequency domain are combined together to yield a single vector *wave equation* [29] in terms of the electric field E or, alternatively, the magnetic field H , as follows:

$$\nabla \times \frac{1}{\mu_r} \nabla \times E - k_0^2 \epsilon_r E = ik_0 Z_0 J \quad (1)$$

In Eq. (1), J is the current density; ϵ_r and μ_r denote, respectively, the relative permittivity and magnetic permeability of the medium. $k_0 = 2\pi f \sqrt{\mu_0 \epsilon_0}$ and $Z_0 = \sqrt{\mu_0 / \epsilon_0}$ are the propagation constant and characteristic impedance of free space. Using either the variational approach [30] or the method of weighted residuals [31,32], we found that Eq. (1) and its dual on the magnetic field can be cast in a matricial form, $\underline{\mathbf{A}} \cdot \mathbf{x} = \mathbf{b}$. The vector \mathbf{x} contains the unknown spatial components of the electromagnetic field, whereas the known vector \mathbf{b} is determined on the basis of boundary conditions and forced excitation. The coefficient matrix $\underline{\mathbf{A}}$ is square, sparse, and symmetric, whose elements indicate the material properties at the nodes. Once such a system of equations has been set up, its solution is achieved by the application of an iterative or direct solving technique [33]. Direct methods are suited for reduced size problems only, because they are computationally very demanding. In typical problems regarding realistic 3-D optical devices, iterative method-based procedures are widely used by virtue of the efficient handling of sparse linear systems [34]. It must be emphasized that the mesh generation within FEM can be cumbersome for large three-dimensional structures (e.g., large amount of random access memory (RAM) needed) [35], and, indeed, mesh setup times exceeding the solution time of the electromagnetic problem have been outlined in the scientific literature.

In FEM, besides tetrahedrons, conformal elements can also be deployed to better approximate curved geometries. In this way, an accurate modeling of inhomogeneous materials and complex nonconformal geometries can be achieved in a straightforward manner [30]. Such flexible meshing capability is a clear advantage over FDTD or FIT schemes based on Cartesian meshes; wherein, each cell of the computational lattice is implicitly assumed to be filled with a homogeneous material [15,16], and therefore a staircase approximation of the morphology has to be used. Another appealing feature of FEM is the simple handling of arbitrary wavelength-dependent relative permittivity of the materials simulated. Furthermore, optical effects occurring at corrugated metal surfaces or metal nanoparticles can be efficiently modeled with FEM. It is worth mentioning that FEM-based algorithms feature a reduced frequency scaling of the computational burden compared to the other methods [36], making the calculations, in a 3-D space, with this method very fast, provided that an adequate amount of RAM memory is available. Finally, FEM can be easily used for accurate multiphysics simulations, providing the capability to couple the

electromagnetic field-based characterization with, for instance, mechanical or thermal modeling [37]. Such a feature allows the enhanced modeling of solar cells with dispersive materials that have temperature-dependent electrical properties [38]. The FEM is a good choice for solving the electromagnetic problems over complicated structures. The method appears to be very effective also for evaluating the optical situation in thin-film photovoltaic devices [39].

2.2. Software

In this work, we use a commercial implementation of FEM, HFSS [40,41], whose optimized algorithm is also capable of solving 3-D electromagnetic problems at optical frequencies. By taking advantage of multicore architectures and providing a wide range of boundary conditions as well as symmetry capabilities, we found that the HFSS performs simulations within a short time. Furthermore, its graphic user interface allows an easy computer-aided design of complex structures. The HFSS runs on a relatively inexpensive workstation (dual six-core X5670 Intel Xeon architecture equipped with 24 GB DDR3-1333 type RAM memory).

Once the simulation of the design (structure, boundary conditions, excitation(s), and frequency range) is set up, FEM-based algorithms in HFSS operate through three phases: *meshing*, *solving*, and *sweeping*. In the first phase, for a given wavelength, the volume of the design is discretized in tetrahedrons. During the second phase, the resulting system of equations, $\underline{\mathbf{A}} \cdot \mathbf{x} = \mathbf{b}$, is iteratively solved. In any iterated steps, the volume of the design is approximated more thoroughly by raising the number of tetrahedrons. If the difference between the values of x_i calculated at the i -th iteration step and the values of x_{i-1} calculated at the $(i-1)$ -th iteration step is smaller than a certain threshold value, the iteration stops, and the system of equations is considered *converged*. From this state, the last phase starts, during which the electromagnetic field in the meshed volume for each frequency previously set up is calculated. Therefore, once the initial frequency is specified, each simulation solves at least two iteration steps before starting the frequency sweep. To improve the numerical stability of the simulations reported in this article, we set the sweeping phase to start only after at least three converged iteration steps in a row.

3. RESULTS

3.1. 3-D modeling of pin thin-film silicon solar cells

Thin-film silicon solar cells present a special optical system with relatively thick layers (micrometer range for transparent conductive contacts or even millimeter range for the substrates) and ultrathin layers (a few nanometer-thick buffer layers or 10-nanometer thick doped layers). This implies that a variable mesh should be applied if

one wants to include thick layers in the simulation effectively. Additionally, according to the coherent length of solar irradiation (in the range of micrometers), one has to consider a coherent propagation of light in thin layers of the solar cell structure. In *pin* solar cells, light is propagated through a thick incoherent glass layer first [42,43]. Despite the adaptable meshing capabilities, such large thicknesses would require plenty of excess computer memory and computational time, although its optical effect is not predominant when studying the trends regarding periodic gratings in thin-film solar cells. Therefore, we follow the approach where the incident light is applied from glass semi-infinite media, neglecting (but being aware of) some effects related to the front and back reflection at the first air/glass interface, which is not included in simulation.

3.2. Setting boundary conditions of the simulated structure

Thin-film solar cells and modules have layered structures with very large transverse size. However, by setting proper boundary conditions, only small segments can be included in the analysis. In this way, the volume to be simulated by the design is reduced to a so-called unit cell. Here, the unit cell serves as the problem domain for boundary conditions, extending the computational volume along the Cartesian coordinate directions x , y , and z (see Figure 1). The boundary conditions used in our simulations can be divided into three groups: (i) the master–slave (M-S) boundary condition [44] acting on surfaces parallel to xz -planes or yz -planes; (ii) the Floquet ports (FPs) [45] acting on

surfaces parallel to the xy -plane; and (iii) the Perfect E–Perfect H (PE–PH) conditions that handles properly the symmetry of cross-sectional surfaces [46].

The M-S is a boundary condition enforced between two parallel surfaces in order to mimic the periodicity along their normal direction. The components of the electromagnetic field determined at the *master* surface are equalized with those at the *slave* surface. In general, *slave* components are phase shifted with respect to the *master* components, according to the distance between the two linked boundary surfaces (d_{M-S}). Such phase shift Φ depends also on the direction of the incident field exciting the simulated structure:

$$\Phi = \frac{d_{M-S}}{\lambda} \sin\theta \cos\phi \quad (2)$$

with the polar angles θ and ϕ indicating the direction of the incident field propagation vector. In our numerical investigations, the phase difference Φ has been set to zero in order to consider only the perpendicular incidence of the incident field, although the scattering processes occurring inside the unit cell are rigorously taken into account. The FPs are adopted at the top and bottom horizontal surfaces of the unit cell as efficient absorbing boundary conditions, often replacing the used perfect matched layers (PML) [46]. Using FPs, we can simulate infinite media in which light propagates almost without reflection to infinity. We found out that FPs are a better solution than the PML-based approach because (i) a smaller volume has to be meshed (i.e., faster simulations) and (ii) a straightforward calculation of reflectance in the

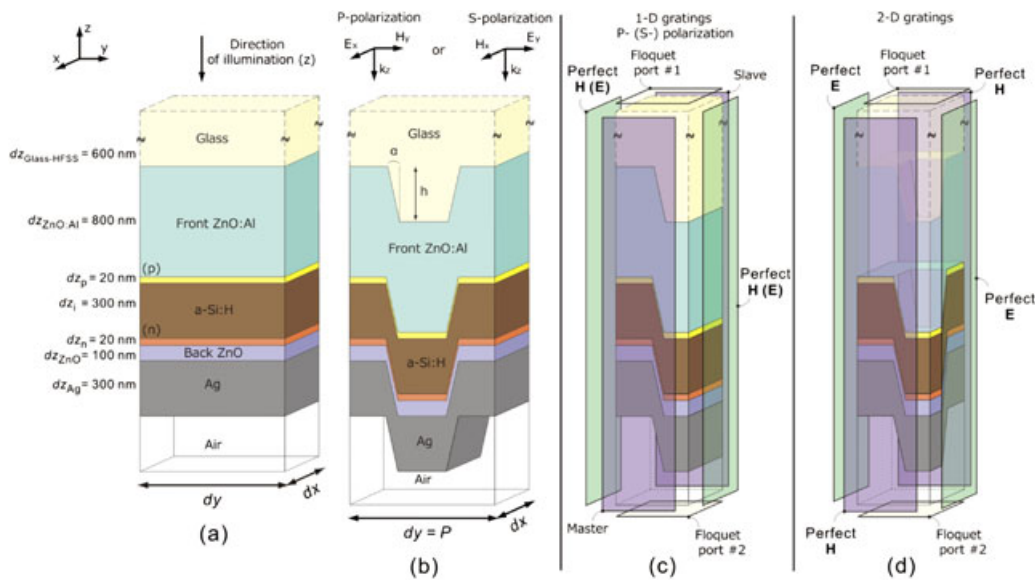


Figure 1. Schematic structures (unit cells) of thin-film silicon solar cells on (a) flat glass and (b) on 1-D gratings. Modeled solar cells that used the symmetry approach on (c) 1-D gratings (M-S, FPs, and PE boundary conditions for P -pol and S -pol) and (d) 2-D gratings (FPs, PE, and PH boundary conditions). The geometrical dimensions dx , dy , and dz (layers thicknesses) define the size of the design (dimensions are not in scale). The period P , the height h , and the slope α of the 1-D gratings are also reported.

simulated structures can be carried out. The FPs approach allows the use of plane waves as a source of excitation. Symmetry conditions PE-PH are used to reduce the volume to be meshed into half for 1-D gratings and into a quarter for 2-D gratings. This approach leads to a much smaller matrix \underline{A} and, consequently, to shorter computational times and to a lower amount of needed RAM. The PE-PH symmetry boundary condition is used for the E field perpendicular (tangential) to the symmetry surface [46].

If FPs are used only at the top and bottom horizontal surfaces of the unit cells, M-S and PE-PH boundary conditions are applied to pairs of parallel vertical surfaces. Therefore, a combination of the conditions is required for simulating solar cells on 1-D or 2-D gratings. Referring to Figure 1(c) and defining the parallel polarization (P -pol) with the E field oriented along the x -direction and the perpendicular polarization (S -pol) with the E field oriented along the y -direction, in case of a solar cell on 1-D gratings investigated for S -pol, the M-S relationship is set between surfaces parallel to yz -plane, whereas a Perfect E symmetry condition is applied at surfaces parallel to xz -planes. For the P -pol case, there is the same M-S relationship, but a Perfect H symmetry condition is used. Regarding the structures based on 2-D gratings (see Figure 1(d)), because they have two symmetry planes, two pairs of symmetry conditions are set up.

3.3. Determination of the input parameters of simulations

The FEM algorithms are able to use measured wavelength-dependent complex refractive indexes ($\tilde{n} = n + ik$), which describe the optical properties of the layers. The real part of the refractive index (n) and the extinction coefficient (k) of the materials used in the presented simulations are shown in Figure 2 and were determined with the use of variable angle spectrometry [47,48]: aluminum-doped zinc-oxide (ZnO:Al), p -doped amorphous silicon-carbide (p -a-SiC:H), intrinsic amorphous silicon (a-Si:H), n -doped amorphous silicon (n -a-Si:H), undoped zinc-oxide (ZnO), and Ag layer.

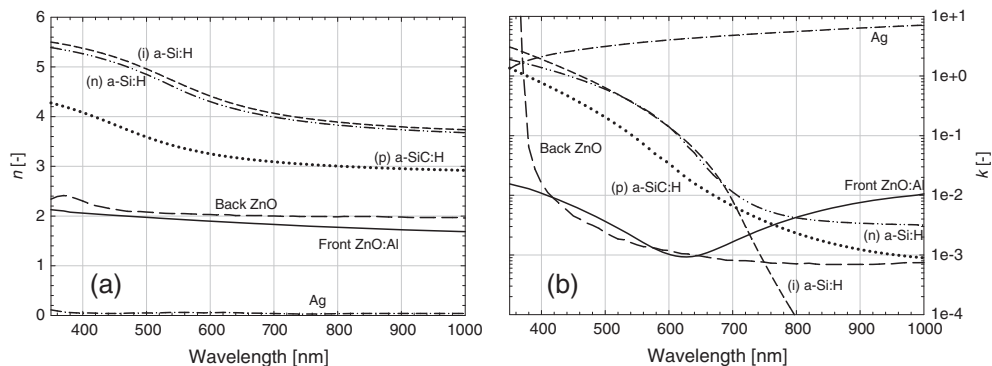


Figure 2. (a) Real part of the refractive index n and (b) the extinction coefficient k of all the materials used.

In order to import the actual surface morphology of the periodic gratings, atomic force microscopy (AFM) was used to characterize the surface of the samples. In our case, the gratings were scribed in lacquer spun onto the glass substrate, following a BluRay Disc™ technique [49]. Because the adopted lacquer features optical properties similar to glass, they were considered as a one-layer substrate with optical properties of glass. In Figure 3, we present a measured transverse cross-section of 1-D grating, which was implemented in our real device for verification purposes (see Section 3.6 for verification). We determined the period, the height, and the duty cycle of the rectangular-like 1-D grating to be 600 nm, 300 nm, and 50%, respectively. The average slope of the steep vertical segments was 9° . In Figure 3, the shape used in simulations is shown by dashed line. Such a slight trapezoidal shape with the same slope $\alpha = 9^\circ$ was used as the approximation in our model. Incorporating realistic optical constants of all layers of the structure and considering textured morphologies of interfaces present an important advantage of our 3-D modeling approach.

3.4. Determination of solar cell optoelectronic output parameters from optical simulations

In our modeling approach, the simulated structure is treated in the HFSS as a two-port high-frequency device [50]. The total reflectance, which is an output parameter of the simulation, can be straightforwardly calculated in terms of S -parameters [50] as $R = |S_{11}|^2$. For the calculation of the absorptance in individual layers, the squared magnitude of the electric field E was integrated over the volume of the film, according to Eq. (3):

$$A_i = \frac{1}{2} \varepsilon_0 \text{Im}(\varepsilon_i) \omega \int_{V_i} |E|^2 dV \quad (3)$$

where ε_0 is the dielectric constant of vacuum, $\varepsilon_i = \tilde{n}_i^2$ is the complex relative permittivity of the i -th material ($\text{Im}(\varepsilon_i) = 2n_i k_i$), and $\omega = 2\pi c/\lambda$ is the angular frequency. The

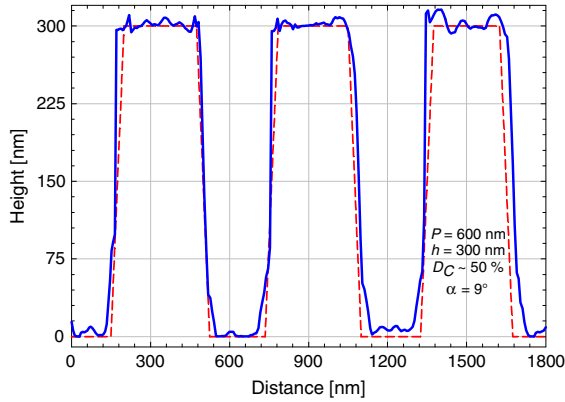


Figure 3. Transverse cross-section of the 1-D grating under test. The dashed red trapezoidal profile represents the approximation used in the model.

transmittance T is generally numerically negligible, because of A_g at the back side of the solar cell.

By convoluting the absorptance A_i with the reference photon flux $\Phi(\lambda)$ of air mass 1.5 [51] in the considered wavelength range (350 nm–1000 nm), the photocurrent density or integrated optical losses generated in the i -th layer (J_{ph-i}) can be calculated as follows [27]:

$$J_{ph-i} = -q \int_{350nm}^{1000nm} A_i(\lambda) \Phi(\lambda) d\lambda \quad (4)$$

where q is the elementary charge. In the hypothesis that each photon absorbed in the a-Si:H i -layer creates an electron–hole pair and such a pair is collected at the electrodes (i.e., neglecting recombination loss mechanisms), the photocurrent density $J_{ph-a-Si:H}$ can be equalized to the short-circuit current density (J_{SC}) of the solar cell.

3.5. Validation of the simulator

For the validation of our modeling approach that used the HFSS software and the correctness of applied boundary conditions, a simple case of flat solar cell was studied first. Such a solar cell was simulated also with 1-D simulator ADVANCED SEMICONDUCTOR ANALYSIS (ASA) which is widely used in simulations of thin-film silicon solar cells [52–54]. The simulated structure, shown in Figure 1(a), comprises of glass substrate, ZnO:Al in the role of front transparent conductive oxide (TCO), amorphous silicon layers forming the p - i - n junction, ZnO as back TCO, and Ag back contact. In the HFSS, we considered the unit cell to be of lateral size $dx = dy = 600$ nm, whereas the thicknesses of the layers were the same as specified in the ASA (see specifications of layer thicknesses in Figure 1(a)). In the case of 3-D HFSS simulation, the light source (plane wave) was applied at the top border, inside the glass medium, and at a distance from the glass/front TCO interface of 600 nm. In the case of the ASA simulations,

we applied the illumination (i) at the same distance from glass/front TCO interface and taking the glass as an incident medium, and (ii) in air where we considered a 0.6-millimeter thick incoherent glass layer. With the example (ii), we want to show the role of front air/glass interface in the analyzed solar cell.

As shown in Figure 4, the reflectance (R) and absorptance in the i -layer ($A_{a-Si:H}$), which were carried out with the HFSS and the ASA (incident medium glass), follow each other in intensity and in the position of the interference fringes, thus, demonstrating that the assumption of thin glass layer made within the carried out HFSS simulations leads to a reasonably accurate modeling of propagation of light in glass medium. The average percentage difference between the spectra is limited to 0.08% for the absorptance and 0.24% for the reflectance. The results of the second simulation case with ASA, where a 0.6-millimeter glass was considered and the light applied in an air medium, revealed no significant differences in the R and $A_{a-Si:H}$ curves. The changes may arise when scattering is accounted for in the solar cell structure, because back scattered rays may experience total reflection at front glass/air interface. However, one may infer that neglecting this interface can result in a reduction of about 4% of the total reflectance (upon assuming a refraction index of $n = 1.5$ for the glass layer), although a minor impact is expected on the trends regarding the improvements in J_{SC} for different gratings that we will analyze further.

3.6. 3-D simulation of pin a-Si:H cell on 1-D gratings and verification with a realistic cell

After testing the flat solar cell, a 1-D grating-textured *pin* cell was simulated in the HFSS.

The layers of the cell and their thicknesses were the same as in the flat case. In the presented simulations, we assume that the texture of the substrate is ideally transferred to all internal interfaces of the cell (conformal growth of layers [8,55]). In Figure 1(b), one period of the

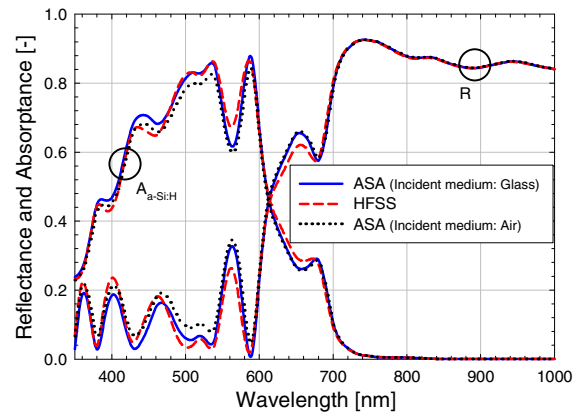


Figure 4. Reflectance (R) and Absorptance ($A_{a-Si:H}$) in the i -layer for the flat solar cell calculated by the HFSS and ASA (air and glass as incident media).

simulated structure is shown. However, the structure with half of the period ($P/2$) was taken as unit cell (see Figure 1(c)) after selecting the right boundary conditions, as explained in Section 3.2. The geometrical characteristics of such a unit cell are $dy = P/2 = 300$ nm, $h = 300$ nm, $D_C = 50\%$, and $\alpha = 9^\circ$. Individual simulations were performed for each polarization (P -pol and S -pol), because 1-D gratings can excite different propagation modes [12,55] depending on the polarization of the incident field.

Different dimensions along the x -direction ($dx = 24$, 60 and 600 nm) were checked without finding any significant difference in the simulation spectra carried out. The choice of $dx = 60$ nm resulted to be optimal as far as memory occupancy, computational time, and correctness of simulation are concerned. Furthermore, testing the same solar cell structure on 1-D gratings without taking advantage of the symmetry ($dx = 60$ nm, $dy = 600$ nm), we obtained identical results for $dy = 300$ nm, corresponding to $P/2$, but within longer computational time. Figure 5 shows the meshed volume of the design solved for the case of S -pol. By choosing the automatic determination of the mesh, we found that the HFSS was able to create a variable mesh, making it finer or coarser depending on the refractive index of the materials (higher n led to smaller tetrahedrons) with p -type and n -type layers well represented by tetrahedrons generated on the steep walls. Details and restrictions of automatic meshing can be found in [46]. Although no special effort was put to obtain a minimal reliable meshing for the case

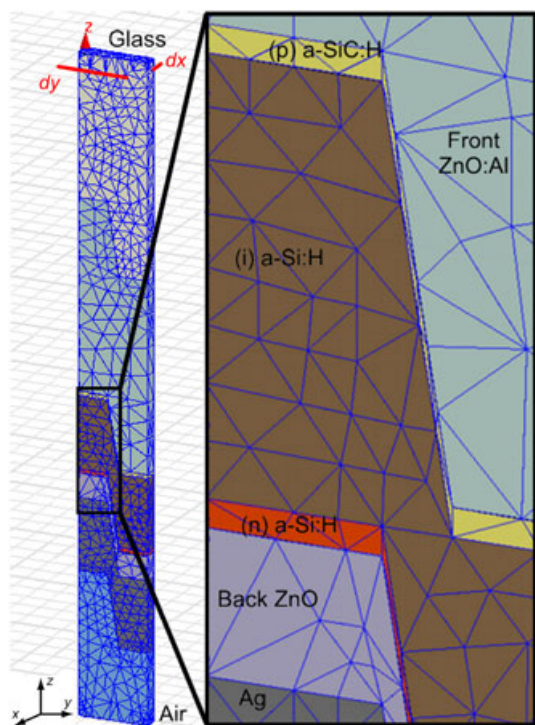


Figure 5. Screenshot of the meshed design for S -pol. The design reported here is $dx = 60$ nm, $dy = 300$ nm (the system of Cartesian coordinates is the same as in Figure 1). The inset shows a detailed zoom of the pin junction.

of thin-film silicon solar cell, we did an additional simulation to prove the accuracy of our choice. We forced the edge length of mesh elements to range from 2–20 nm according to the electrical properties and geometrical characteristics of the different dielectric layers forming the solar cell. In this way, one can achieve a good numerical accuracy of the FEM-based solving procedure, at the same time trying to keep reasonable computational times. As a matter of fact, the output spectra from such a simulation were identical to those of the simulation run with automatic meshing, although, resulting in solving times of up to 30 times longer and memory occupancy of up to 50 times higher.

For the verification of the proposed optical modeling, a single junction solar cell was fabricated as an experimental reference, employing our established process for cell fabrication on periodic textures [7]. The solar cell was deposited on 1-D gratings with the use of the radio frequency plasma enhanced chemical vapor deposition technique in pin configuration. Front and back TCO layers were deposited using the rf-magnetron sputtering; silver was evaporated through the physical vapor deposition. The solar cell had the following configuration: glass/1-D grating (see Section 3.3)/front ZnO:Al contact (800 nm)/ (p) a-SiC:H (20 nm)/ (i) a-Si:H (300 nm)/ (n) a-Si:H (20 nm)/ back ZnO (100 nm)/ Ag contact (300 nm). The external quantum efficiency (EQE) was measured using unpolarized monochromatic light from 300 nm to 800 nm. For this reason, the simulated spectra presented in this section are the average between the simulation results of P -pol and S -pol. The total reflectance of the solar cell was measured using a spectrophotometer equipped with an integrating sphere.

The simulated $A_{a-Si:H}$ and the measured EQE of the solar cell on 1-D gratings are reported together in Figure 6(a). For wavelengths shorter than 560 nm, the EQE of the fabricated textured pin solar cell is smoother than the simulated $A_{a-Si:H}$ as a consequence of the growth of sputtered ZnO:Al on 1-D gratings, which introduces nanoscale features [7] (effect not taken into account in this model). For wavelengths larger than 560 nm, the two curves present a similar behavior, especially for the presence of the peaks at 600 nm and 660 nm. The slight shift of the first peak in the EQE of the measured cell on 1-D gratings, with respect to the simulated one, may be due to a little difference in the thickness of the deposited i -layer on textured morphology. The lower amplitude of both peaks in the measured cell indicates that the height of the gratings was not preserved during the thin-films deposition [7]. In Figure 6(b), the measured and simulated 1- R and i -layer absorptance are reported. It is noticeable that also the simulated reflectance closely follows the measured one. The good agreement between measured and calculated 1- R and EQE spectra provides basic confidence for further analysis of the simulation results.

3.7. Analysis of simulation results of a-Si:H cell on 1-D gratings

For short wavelengths and with respect to the absorptance of the simulated flat solar cell, also reported in Figure 6(a),

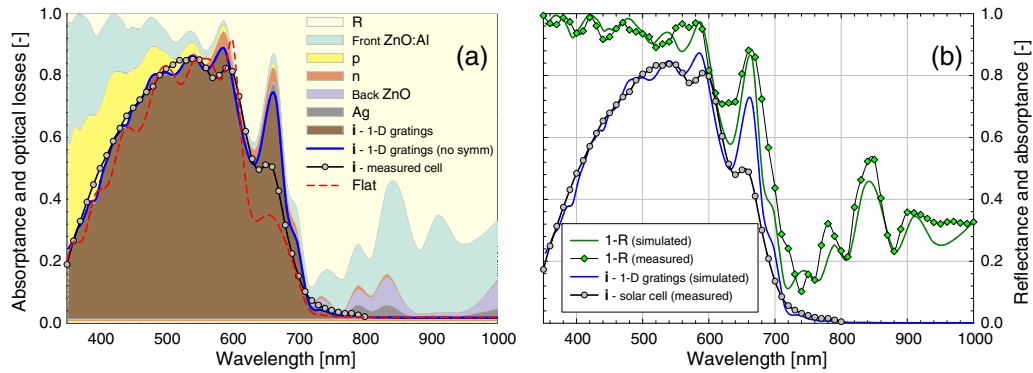


Figure 6. (a) Simulated i -layer absorbance and optical losses for a solar cell on 1-D gratings ($P/2 = 300$ nm, $h = 300$ nm). The circled black line is the measured EQE of the solar cell on 1-D gratings; the dashed red line is the absorbance of the flat cell (see Figure 4); and the blue line indicates modeled absorbance with no symmetry ($P = 600$ nm, $h = 300$ nm). (b) Comparison between the 1- R and i -layer absorbance, which are measured and simulated.

the solar cell on 1-D gratings presents smoothened interference fringes, resulting in a pronounced antireflective effect. For longer wavelengths, the textured cell presents greater absorption than in the flat case, clearly showing the scattering effect of the diffraction gratings.

In Figure 7, the photocurrent densities (J_{ph}), related to absorption in i -layer (actual J_{SC} of the cell) and to losses caused by reflected light from the structure and absorbed light in the supporting layers, are given for the two simulated cells. The antireflective effect given by the 1-D gratings decreases the current density loss level because of the reflectance (net difference of 3.98 mA/cm² from flat glass to 1-D gratings), but it also increases the current density absorbed into the front ZnO:Al (+32.18%), illuminated not only from its front side (scattered photons at the glass/ front TCO interface) but also from its back side (diffuse reflectance at the front TCO/ p -layer interface). Also, cells in the nip configuration, deposited on the back substrate with gratings texture, suffer from this

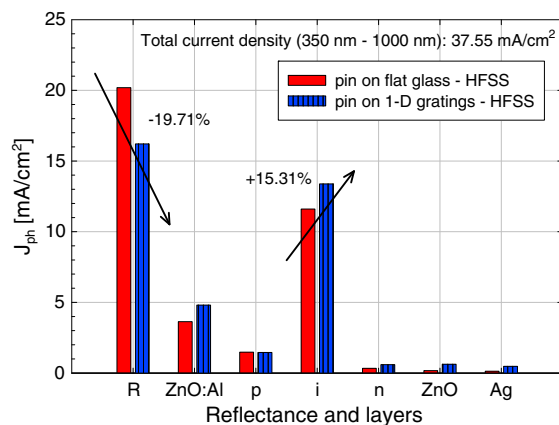


Figure 7. Photocurrent densities integrated over the chosen wavelength range (350–1000 nm). Percentage values are calculated with respect to the flat cell.

problem [11]; but in the pin technology, the front TCO is generally thicker, thus, causing higher parasitic absorption. In the pin junction area, the p -type layer absorbs slightly less than in the flat case, because of the fact that fewer ultraviolet photons arrive in this layer, having already been absorbed by the front TCO. Thanks to the scattering effect of the gratings and their antireflective action, the active i -layer delivers 15.31% more current density than in flat case. In the next section, we show that it is possible to obtain better performance by choosing other combinations of geometrical features and/or switching from 1-D to 2-D gratings. Together with the n -type layer, the back ZnO constitutes an increased source of losses with respect to the pin flat cell because of the scattering provided by the gratings. Finally, also the textured silver back contact shows parasitic absorption, which is anyhow mitigated by the presence of the back ZnO [27].

Looking at S -pol and P -pol individually offers the interpretation of the features present in the averaged spectra of the simulated pin cell on 1-D gratings. Figure 8(a, b) shows the reflectance and absorbances of i -layer, front and back TCO, and Ag for S -pol and P -pol, respectively. We divide the wavelength range into three regions: (i) from 350 nm to 600 nm, (ii) from 600 nm to 700 nm, and (iii) from 700 nm to 1000 nm. In Figure 9, electric field magnitude spatial distributions are reported for representative wavelengths of the three regions (500 nm, 652 nm, and 700 nm). The results in Figures 8 and 9 will be compared at the same time. In the first region, the absorbances corresponding to S -pol and P -pol are very similar and only slight differences in the amplitudes can be observed, such as the small oscillations in P -pol case. Also, the electric field magnitude spatial distribution for both polarizations, shown in Figure 9(a), confirms such a trend. In the second region, the effect of the polarizations in the solar cell structure is already clearly visible. Switching from S -pol to P -pol, we found that the reflectance peak at 640 nm seems to shift towards shorter wavelengths (625 nm) and another one occurs at 680 nm. Similarly, the absorbance peak in the

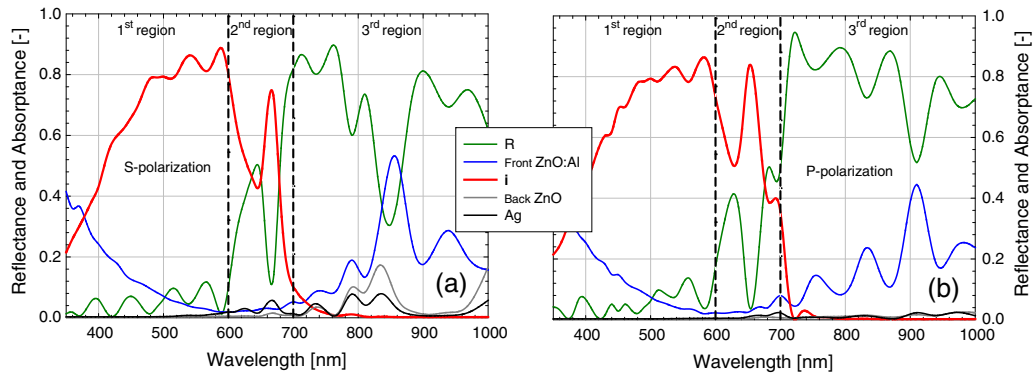


Figure 8. Comparison between the *i*-layer spectral response, reflectance, and main parasitic absorptances for (a) S-pol and (b) P-pol. Vertical dashed lines delimit the discussed three regions.

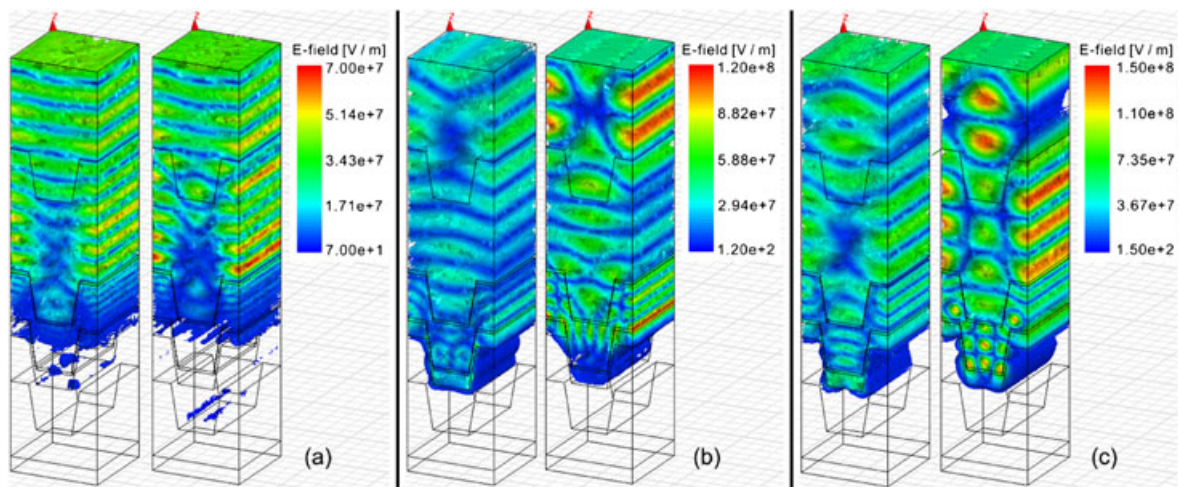


Figure 9. Electric field magnitude spatial distribution at three wavelengths for S-pol (left) and P-pol (right): (a) 500 nm, (b) 652 nm, and (c) 700 nm. The system of Cartesian coordinates is the same as in Figure 1. The pictures reported here refer to a bigger design ($dx = 600$ nm and $dy = 600$ nm) for visualization purposes.

i-layer at 670 nm shifts to 660 nm, whereas the other two peaks appear at 690 nm and 740 nm. For the selected wavelengths, in Figures 9(b, c), the lower intensity of the electric field magnitude in S-pol indicates smaller absorptance and higher reflectance than the P-pol case. The outlined physical behavior is actually because of the enhanced excitation of propagation-guided waves within the grating substrate of the solar cell under S-polarized light illumination. The wave guidance phenomenon results in a more efficient light focalization and trapping effect and, hence, is superior in performance in terms of external quantum efficiency (i.e., energy absorption) compared to the case of P-polarized light excitation [12,26]. In the third region, where the extinction coefficient of the a-Si:H becomes the smallest among all the other layers (see Figure 2(b)), the absorption is mainly within the silver, the front, and the back TCO, whereas the reflectance constitutes the rest. However, for P-pol, the absorption in the back ZnO and Ag is smaller than in S-pol case. This is because of a deep feature at 850 nm for the reflectance

in the S-pol case. In the closest range of this wavelength, the optically parasitic layers resonate, thus, increasing their absorptance. In Figure 10, the local absorptance in the layers at 830 nm is shown, and, as expected in Figure 8, in the S-pol case, the absorption is higher than in the P-pol case. In Table I, the J_{ph} calculated for each layer and for both polarizations are reported. In the P-pol case, the J_{ph} of the reflectance and of the absorptance of the front ZnO:Al is more pronounced than in the S-pol. For all the other layers, either there is no difference (*p*-layers and *n*-layers) between polarizations, or there is a higher response for the S-pol.

3.8. 3-D simulation of a-Si:H cell on 2-D grating textures and comparison with 1-D textures

3-D optical simulators, in contrast to 2-D simulators, enable the simulation of structures with variations applied in both *x*-directions and *y*-directions. We employed our

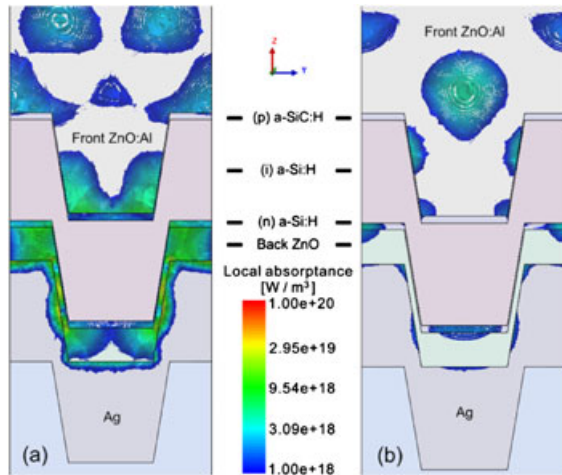


Figure 10. Local absorbance in the simulated structure at 830 nm for (a) S-pol and (b) P-pol simulations.

3-D simulator in simulating a *pin* a-Si:H solar cell on 2-D grating textures. After that, a comparison of geometrical dimensions (P and h) of 1-D and 2-D gratings for optimal J_{SC} was carried out.

Referring to the structures depicted in Figure 1, we proceeded with the simulation of a 2-D grating-textured solar cell with boundary conditions described in Section 3.2. Materials and thicknesses of the layers were kept identical as in the case of the flat and 1-D gratings-textured solar cell, as well as the period ($P/2=300$ nm) and the height ($h=300$ nm). Because 2-D gratings are invariant with polarization, only one simulation was needed to determine the optical situation inside the solar cell. In Figure 11, the absorbance in the *i*-layer and the optical losses related to the 2-D gratings solar cell are reported, together with the $A_{a-Si:H}$ of the flat and 1-D gratings-textured solar cells. Upon comparing the absorbances in the *i*-layers at short wavelengths, the switch from 1-D to 2-D gratings does not result in further improvements, with respect to the flat cell. Actually, for this combination of period and height, the 1-D gratings solution supply more pronounced antireflective capabilities compared to the 2-D gratings

Table I. J_{ph} [mA/cm²] in each layer for flat and textured *pin* cells (average and polarizations).

Layers	Flat	Textured		
		Average	S-pol	P-pol
<i>R</i>	20.99	15.67	14.82	16.53
ZnO:Al	2.24	4.87	4.61	5.14
<i>p</i>	1.62	1.24	1.20	1.28
<i>i</i>	11.54	13.80	14.08	13.52
<i>n</i>	0.30	0.68	0.66	0.70
ZnO	0.07	0.60	1.05	0.14
Ag	0.81	0.67	1.11	0.24
Total	37.55	37.55	37.55	37.55

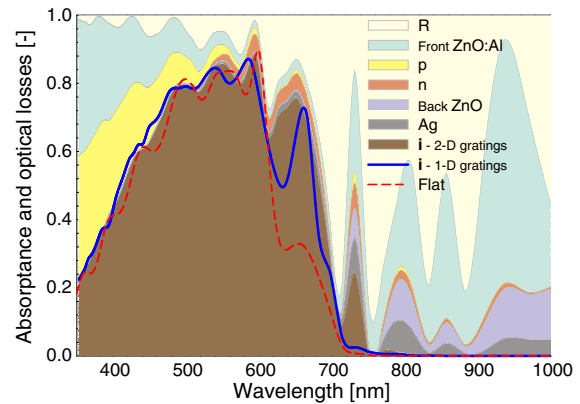


Figure 11. Simulated absorbance in *i*-layer and optical losses for solar cell on 2-D gratings ($P/2=300$ nm, $h=300$ nm). The blue line indicates absorbance in the *i*-layer for the solar cell on 1-D gratings ($P/2=600$ nm, $h=300$ nm); the dashed red line is the absorbance of the flat cell (see Figure 4).

solution. However, for wavelengths longer than 600 nm, the solar cell on 2-D gratings experiences a stronger scattering with the broad peak around 650 nm and a new one located between 700 nm and 750 nm. The peaks related to the parasitic absorptions in the back TCO and Ag layers are also remarkable. In Figure 12, we report the photocurrent densities related to the total reflectance and absorbances for the three simulated solar cells. By using 2-D gratings, a further decrease of the optical losses caused by the reflectance (from -19.71% of 1-D gratings to -40.77% of 2-D gratings, with respect to flat cell), as well as a general increase of absorbance in all other layers, are achieved. Textured with 2-D gratings, the *i*-layer delivers 24.42% more current ($+2.83$ mA/cm²) than in the flat case.

After our preliminary simulation of 2-D grating-textured solar cell, we introduced the variation of P and h for 1-D and 2-D gratings in order to find a geometrical

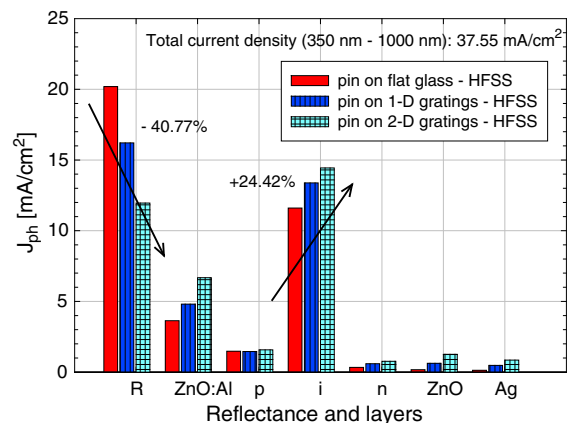


Figure 12. Photocurrent densities integrated over the chosen wavelength range (350–1000 nm). Percentage values refer to the solar cell on 2-D gratings and are calculated with respect to the flat cell.

combination capable of delivering optimal J_{SC} for *pin* a-Si:H solar cells. The P was varied in discrete steps from 300 nm to 1000 nm, the h from 150 nm to 450 nm, and the D_C was kept constant at 50%. The slope α was linearly varied with the P at a rate of $-1.54/100$ nm. In this respect, for example, the simulated structures with $P=300$ nm (1000 nm) have $\alpha=4.38^\circ$ (15.16°). In our simulations, we found out that the optimal combination of P and h for 1-D and 2-D gratings does not change when the slope α is varied or kept constant. However, α affects the J_{SC} values. In addition, we ran test simulations of structures on 2-D gratings with and without symmetry planes, obtaining the same reflectance and absorptance spectra.

Results of our investigation are summarized in Figure 13 (a), where the J_{SC} is used as a figure of merit to indicate the best combination of P and h for 1-D and 2-D gratings with respect to the flat interfaces, and in Figure 13(b), where the current density related to reflectance (J_R) is used to quantify the antireflective effect. As previously mentioned, in the case of 1-D gratings, the J_{SC} values were calculated from the averaged absorptance spectra obtained from the *S*-pol and *P*-pol simulations. The reported trends of the J_{SC} for different heights are similar. Even though the period 400 nm is the most effective for all the heights, in the case of $h=450$ nm, the influence of the P is not as significant as in the other two investigated heights. The optimal combination for this type of texture is $P=400$ nm and $h=300$ nm, resulting in a percentage increase of +25.46% in J_{SC} , with respect to the flat cell. Switching to the 2-D grating case, the trends of J_{SC} are again similar

for the three heights, generally performing better than their 1-D grating counterparts. However, for smaller heights and large periods, the 1-D gratings work remarkably better than the 2-D gratings above all the combination $P=1000$ nm and $h=300$ nm. For the 2-D gratings, the structure with period 500 nm delivers the largest J_{SC} for all the heights, and the optimum is obtained at $h=450$ nm. With this configuration, the percentage increase in J_{SC} is found to be +32.53%, with respect to the flat cell.

The values of J_R resulted from the convolution of the simulated reflectance curves with the AM1.5 photon flux over the entire wavelength range 350–1000 nm. As shown in Figure 13(b), all the combinations based on 2-D gratings generally exhibit better antireflective effect with respect to their counterparts on the basis of the 1-D gratings. In the considered wavelength range, the antireflective effect given by the best 2-D grating is better than that of the best 1-D grating. In more detail, the values of J_R from the 1-D gratings hardly move from 15 mA/cm², whereas those from 2-D gratings show dependency on period and height with minima located around the period 500 nm and inversely correlated with the maxima found in the J_{SC} .

Within the parameter space investigated, the textured cells always performed better than the flat one, indicating that diffraction grating textures own a realistic potential to increase the efficiency of thin-film silicon solar cells. In Figure 14, the spectral responses of the simulated flat cell and the best gratings combinations are compared. Cells on diffraction gratings outperform the flat one with important antireflective and scattering effects throughout

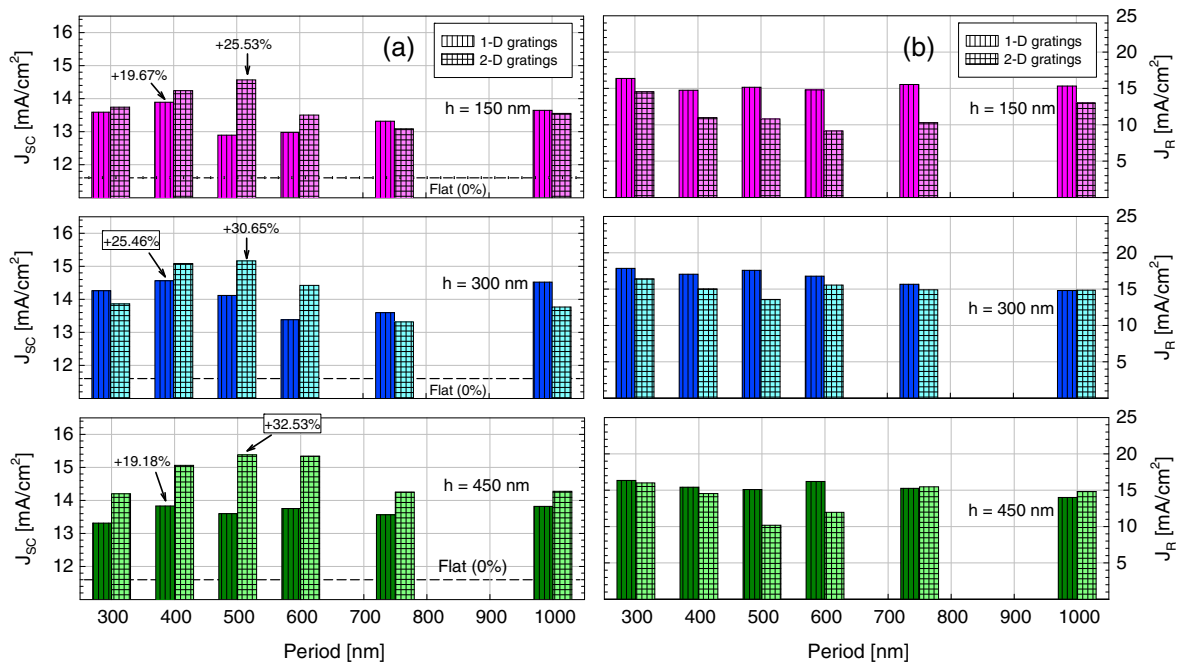


Figure 13. (a) J_{SC} analysis for different periods and heights. Framed values have the highest percentage increases for 1-D and 2-D gratings with respect to the flat cell; (b) current density related to reflectance (J_R) for antireflective effect analysis between 1-D and 2-D gratings with respect to different periods and heights.

the entire wavelength range. The textured solar cells, however, present different relative performances. Even though in the near infrared range the best 2-D grating results to be more efficient, the cell on the best 1-D grating shows a slightly better antireflective effect. This is because of the fact that when using a narrower wavelength range (350–550 nm), the J_R is minimal around the period 400 nm.

4. DISCUSSION

The reliability and the efficiency of the developed 3-D model were successfully assessed in two subsequent steps: (i) validation of the HFSS behavior with respect to ASA software for a simple flat cell and (ii) verification of the simulation results with respect to real solar cell fabricated on 1-D gratings. Thus, it was proved that our 3-D optical model is able to rigorously compare the spectral response and optical losses of thin-film silicon solar cells on diffraction gratings, with respect to a flat cell. A preliminary numerical investigation on the effect of oblique light incidence, not shown in this work for the sake of brevity, has outlined an excellent agreement with the theory. A dedicated study, based on the presented modeling approach, is ongoing and will be presented in future papers. Anyhow, it has to be mentioned that the impact of oblique light incidence on the optical properties of realistic solar cells has already been discussed in some papers, which use FDTD-based methodologies, available in the scientific literature [56,57].

Simulation results demonstrate that, in case of 1-D gratings, polarization plays an important role. Indeed, for wavelengths longer than 600 nm, remarkable differences were found between *S*-pol and *P*-pol. Our 3-D model carried out, for *S*-pol, higher $A_{a-Si:H}$, and parasitic absorptances at the back side of the cell with respect to *P*-pol.

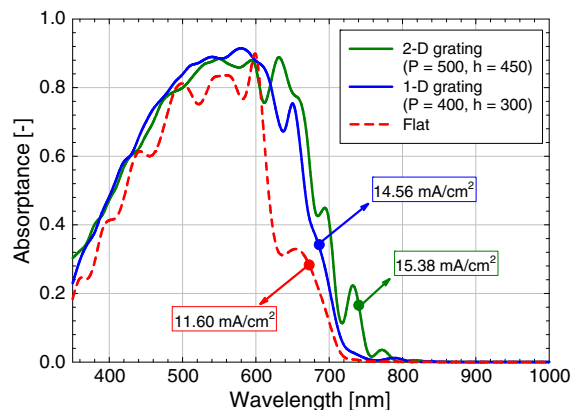


Figure 14. Comparison between simulated absorbances of flat solar cell and the solar cells based on the best 1-D and 2-D gratings combinations; period P and height h indicated are in nm.

Table II. RAM usage and computational time for a selection of simulated solar cells ($h = 450$ nm), MB indicates megabytes. For 1-D gratings, RAM is the sum of the memory used in *S*-pol and *P*-pol simulations.

P [nm]	1-D gratings			2-D gratings	
	RAM [MB]	Time (<i>S</i> -pol) [hr:min:s]	Time (<i>P</i> -pol) [hr:min:s]	RAM [MB]	Time [hr:min:s]
300	655	0:36:24	0:43:39	434	0:35:58
400	763	0:29:38	0:50:10	628	0:46:00
500	438	0:25:08	0:26:24	810	1:25:18
600	451	0:26:16	0:32:16	597	0:52:46
750	659	0:38:29	0:46:19	1330	1:37:25
1000	561	0:38:29	0:32:42	1370	1:46:25

For this, we found [12] an additional experimental verification in literature.

Another important aspect of our investigation is that the optimal combinations of P and h reported in this work are related to a-Si:H-based *pin* solar cells. Changing device structure and using different absorbing materials, such as (micro-crystalline) crystalline silicon, will result in different optimal geometries [27,58].

We evaluated the efficiency of our 3-D model in Table II where the memory usage and the computational times of the biggest simulated solar cells on 1-D and 2-D gratings ($h = 450$ nm) are reported. The amount of used RAM rarely exceeded 1 GB (1 GB = 1000 MB); this instance occurred only for bigger designs based on 2-D gratings. The memory used for 1-D gratings is reported as the sum of RAM in both *S*-pol and *P*-pol simulations, because we actually performed the two simulations in parallel. We found that *P*-pol simulations usually took longer than *S*-pol ones. With average computational times of about 50 minutes, 2-D gratings-textured solar cells could be simulated in a short amount of time, the lengthiest computation taking less than 2 h.

5. CONCLUSION

In this contribution, an effective rigorous 3-D optical modeling of thin-film silicon solar cells was presented. A commercial version of 3-D FEM, the HFSS, was used to simulate the optical response of *pin* thin-film silicon solar cell on 1-D and 2-D gratings. Developing a fast and physically reliable method to simulate such types of solar devices is important not only for the optimization of the gratings for real-life solar cells but also for the study of the scattering processes occurring at textured interfaces.

The model was validated, with the reference software ASA, in the case of the solar cell with flat interfaces on the thick glass. Our optical model allows the simulation of optically thick substrates, such as glass, at the same time designing them to be as thin as the thin-films used in solar cells. This is an important step, as the complexity of the

structure can be kept low, resulting in faster calculations. The simulation of a *pin* cell on 1-D gratings was also described in detail. The results were compared to a real thin-film silicon solar cell deposited on 1-D grating texture. From the comparison of the spectral responses and with the aid of the model, optical losses and polarization dependency could be addressed.

Afterwards, the model was used to carry out the simulation of solar cells on 1-D and 2-D grating textures with different periods and heights, pursuing an optimal combination for the highest J_{SC} . For 1-D (2-D) gratings, such a combination was found to be $P=400$ nm (500 nm) and $h=300$ nm (450 nm), resulting in a percentage increase of +25.5% (+32.5%), more J_{SC} than in the case of the flat cell. From this investigation, all gratings-textured solar cells outperformed the flat ones, showing that diffraction gratings can boost the efficiency of thin-film silicon solar cells.

In view of the inexpensive computer hardware used, tests with physically reliable results could be quickly carried out: for each simulation, the RAM usage was kept as low as 1.5 GB, and the average computational time was about 50 min. With such an interesting technical performance, our model can be profitably used for further optimization studies, opening a new season of 3-D FEM optical modeling in thin-film silicon solar cells.

ACKNOWLEDGEMENTS

This work was carried out with a subsidy from the Dutch Ministry of Economic Affairs under the EOS-LT program (Project No. EOSLT04029). The company MoserBaer is acknowledged for providing the 1-D gratings. The authors thank G. Gentile, D. C. Cortes, T. Temple, and J. Krč for the useful discussions.

REFERENCES

1. Zeman M. *Advanced Amorphous Silicon Solar Cell Technology*, in *Thin Film Solar Cells: Fabrication, Characterization and Applications*, eds. Poortmans J, Archipov V. Wiley: Chichester, 2006; 173–236. ISBN: 978-0-470-09126-5
2. Bailat J, Fesquet L, Orhan J-B, Djeridane Y, Wolf B, Madliger P, Steinhäuser J, Benagli S, Borrello D, Castens L, Monteduro G, Marmelo M, Dehbozorgi B, Vallat-Sauvain E, Multone X, Romang D, Boucher J-F, Meier J, Kroll U, Despeisse M, Bugnon G, Ballif C, Marjanovic S, Kohnke G, Borrelli N, Koch K, Liu J, Modavis R, Thelen D, Vallon S, Zakharian A, Weidman D. Recent developments of high-efficiency Micromorph® tandem solar cells in KAI-M PECVD reactors. *Proceedings of the 25th European Photovoltaic Solar Energy Conference*. Valencia, Spain, 2008; 2720–2723. DOI: 10.4229/25thEUPVSEC2010-3BO.11.5
3. Kambe M, Takahashi A, Taneda N, Masumo K, Oyama T, Sato K. *Proceedings of the 33rd IEEE PVSC: San Diego (IEEE: New York, 2008)*; 1–4. DOI: 10.1109/PVSC.2008.4922507
4. Isabella O, Moll F, Krč J, Zeman M. Modulated surface textures using zinc-oxide films for solar cells application. *Physica Status Solidi A* 2010; 1–5. DOI: 10.1002/pssa.200982828
5. Krč J, Zeman M, Čampa A, Smole F, Topič M. Novel approaches of light management in thin-film silicon solar cells. *Materials Research Society Symposium Proceedings* 2006; **910**: A25-A. DOI: 10.1557/PROC-0910-A25-01
6. Haug F-J, Söderström T, Cubero O, Terrazzoni-Daudrix V, Niquille X, Perregeaux S, Ballif C. *Materials Research Society Symposium Proceedings* 2008; **1101**: KK13-KK. DOI: 10.1557/PROC-1101-KK13-01
7. Isabella O, Čampa A, Heijna M, Soppe WJ, van Erven R, Franken RH, Borg H, Zeman M. Diffraction gratings for light trapping in thin-film silicon solar cells, *Proceedings of the 23rd European Photovoltaic Solar Energy Conference: Valencia, Spain, 2008*; 2320–2324. DOI: 10.4229/23rdEUPVSEC2008-3AV.1.48
8. Söderström T, Haug F-J, Niquille X, Terrazzoni V, Ballif C. Asymmetric intermediate reflector for tandem Micromorph thin film silicon solar cells. *Applied Physics Letters* 2009; **94**: 063501. DOI: 10.1063/1.3079414
9. van Erven AJM, Rutten J, van der Hofstad G, de Groot H, Steltenpool M, De Ruijter J, Titulaer B, Borg H, Rajeswaran G. Light-trapping enhancement by diffractive textures for thin-film silicon solar cells, *Proceedings of the 25th European Photovoltaic Solar Energy Conference: Valencia, Spain, 2010*; 3181–3184. DOI: 10.4229/25thEUPVSEC2010-3AV.2.12
10. Sai H, Fujiwara H, Kondo M. Back surface reflectors with periodic textures fabricated by self-ordering process for light trapping in thin-film microcrystalline silicon solar cells. *Solar Energy Materials and Solar Cells* 2009; **93**: 1087–1090. DOI: 10.1016/j.solmat.2008.12.030
11. Čampa A, Isabella O, van Erven R, Peeters P, Borg H, Krč J, Topič M, Zeman M. Optimal design of periodic surface texture for thin-film a-Si:H solar cells. *Progress in Photovoltaics: Research and Applications* 2010; **18**: 160–167. DOI: 10.1002/pp.940
12. Söderström K, Haug F-J, Escarré J, Cubero O, Ballif C. Photocurrent increase in *n-i-p* thin film silicon solar cells by guided mode excitation via grating coupler. *Applied Physics Letters* 2010; **96**: 213508. DOI: 10.1063/1.3435481
13. Heine C, Morf RH. Submicrometer gratings for solar energy applications. *Applied Optics* 1995; **34**: 2476–2482.

14. Morf RH. Exponentially convergent numerically efficient solution of Maxwell's equations for lamellar gratings. *Journal of the Optical Society of America*. A 1995; **12**: 1043–1056.
15. Yee KS. Numerical solution of initial boundary value problems involving Maxwell's equations. *IEEE Transactions on Antennas and Propagation* 1966; **14**: 302–307.
16. Weiland T. A discretization method for the solution of Maxwell's equations for six-component fields. *Electronics and Communications AEUE* 1977; **31**(3): 116–120.
17. Moharam MG, Gaylord TK. Rigorous coupled-wave analysis of planar-grating diffraction. *Journal of the Optical Society of America* 1981; **71**: 811–818.
18. Gibson WC. *The Method of Moments in Electromagnetics*. Chapman & Hall/CRC: Boca Raton, 2008. ISBN 978-1-4200-6145-1
19. Jin J-M. *The Finite Element Method in Electromagnetics*. 2nd ed. John Wiley & Sons: New York, 2002. ISBN: 978-0-471-43818-2
20. Ansys HFSS official website, <http://www.ansoft.com/products/hf/hfss/>
21. Taflov A, Hagness SC. *Computational Electrodynamics: The Finite Difference Time Domain Method*. 3rd ed. Artech House: Norwood, 2005. ISBN 978-1-58053-832-9
22. Haase C, Stiebig H. Optical properties of thin-film silicon solar cells with grating couplers. *Progress Photovoltaics: Research and Applications* 2006; **14**: 629–641. DOI: 10.1002/pip.694
23. Luebbers RJ, Hunsberger F. FDTD for Nth-order dispersive media. *IEEE Transactions on Antennas and Propagation* 1992; **40**: 1297–1301.
24. Solntsev S, Zeman M. Optical modeling of thin-film silicon solar cells with submicron periodic gratings and nonconformal layers, accepted for publication in Energy Procedia 2011.
25. Solntsev S, Isabella O, Caratelli D, Kyriakou M, Yarovy O, Zeman M. Advanced optical modeling of thin-film silicon solar cells with 1-D periodic gratings. *Materials Research Society Symposium Proceedings* 2011. DOI: 10.1557/opl.2011.1298
26. Naqavi A, Söderström K, Haug F-J, Paeder V, Scharf T, Herzig HP, Ballif C. Understanding of photocurrent enhancement in real thin film solar cells: towards optimal one-dimensional gratings. *Optics Express* 2011; **19**: 128–140. DOI: 10.1364/OE.19.000128
27. Peters M, Rüdiger M, Hauser H, Hermle M, Bläsi B. Diffractive gratings for crystalline silicon solar cells—optimum parameters and loss mechanisms. *Progress in Photovoltaics: Research and Applications* 2011. DOI: 10.1002/pip.1151
28. Tomisawa M, Tokuda M. Induction characteristics of a solar cell to radiated electromagnetic disturbances, *Asia-Pacific Symposium on Electromagnetic Compatibility and 19th International Zurich Symposium on Electromagnetic Compatibility* 2008. DOI: 10.1109/APEMC.2008.4559931
29. Stratton JA. *Electromagnetic Theory*. IEEE Press: Piscataway, 2007. ISBN: 978-0-470-13153-4
30. Ritz W. Über eine neue Methode zur Lösung gewisser Variationsprobleme der mathematischen Physik. *Journal für reine und angewandte Mathematik* 1909; **135**: 1–61.
31. Volakis JL, Chatterjee A, Kempel LC. *Finite Element Method for Electromagnetics: Antennas, Microwave Circuits, and Scattering Applications*. IEEE Press: Piscataway, 1998. ISBN: 0-7803-3425-6
32. Wang JJH. *Generalized Moment Methods in Electromagnetics*. John Wiley & Sons: New York, 1991. ISBN: 978-0471-51443-5
33. Meyer CD. *Matrix Analysis and Applied Linear Algebra*. SIAM: Philadelphia, 2000. ISBN: 0-89871-454-0
34. Saad Y. *Iterative Methods for Sparse Linear Systems*, 2nd ed. SIAM: Philadelphia, 2003. ISBN: 978-0-898715-34-7
35. Nagakura S, Noguchi S, Yamashita H, Cingoski V. Automatic hexahedral mesh generation for FEM using shape recognition technique and tree method, *IEEE Transactions on Magnetics* 2002; **38**: 417–420.
36. Davidson DB. *Computational Electromagnetics for RF and Microwave Engineering*. Cambridge University Press: Cambridge, 2005. ISBN: 978-0-521-51891-8
37. COMSOL, <http://www.comsol.com/products/multiphysics/>
38. Fan JCC. Theoretical temperature dependence of solar cell parameters. *Solar Cells* 1986; **17**: 309–315.
39. Lipovšek B, Cvek M, Čampa A, Krč J, Topič M. Analysis and optimisation of periodic interface textures in thin-film silicon solar cells, *Proceedings of the 25th European Photovoltaic Solar Energy Conference*: Valencia, Spain, 2008; 3120–3123. DOI:10.4229/25thEUPVSEC2010-3AV.1.81
40. White papers in Ansys HFSS official website, <http://www.ansoft.com/products/hf/hfss/>
41. Gentile G, Dekker R, de Graaf P, Spirito M, Pelk MJ, de Vreede LCN, Rejaei Salmassi B. Silicon filled integrated waveguides. *IEEE Microwave and Wireless Components Letters* 2010; **20**(10): 536–538.
42. Milonni PW, Eberly JH. *Lasers*. John Wiley & Sons: New York, 1988. ISBN: 978-047162-731-9
43. Ley L. Photoemission and optical properties. *The Physics of Hydrogenated Amorphous Silicon II Topics in Applied Physics* 1984; **56**: 61–168. DOI: 10.1007/3540128077.3

44. Bardi I, Remski R, Perry D, Cendes Z. Plane wave scattering from frequency-selective surfaces by the finite-element method. *IEEE Transactions on Magnetics* 2002; **38**(2): 641–644. DOI: 10.1109/20.996167
45. Kröner D. Absorbing boundary conditions for the linearized Euler equations in 2-D. *Mathematics of Computation* 1991; **57**(195): 153–167.
46. Ansys HFSS 12, HFSS online help, Technical notes.
47. Sap JA, Isabella O, Jäger K, Zeman M. Extraction of optical properties of flat and surface-textured transparent conductive oxide films in a broad wavelength range. *Thin Solid Films* 2011; **520**(3): 1096–1101. DOI: 10.1016/j.tsf.2011.08.023
48. Van Nijnatten PA. An automated directional reflectance/transmittance analyser for coating analysis. *Thin Solid Films* 2003; **442**: 74–79.
49. <http://www.blu-raydisc.com/Assets/Downloadablefile/BD-ROMwhitepaper20070308-15270.pdf>
50. Gonzalez G. *Microwave transistor amplifiers analysis and design*. 2nd ed. Prentice Hall: Upper Saddle River, 1997: 22–24. ISBN: 978-13581-646-2
51. <http://rredc.nrel.gov/solar/spectra/am1.5/>
52. Dagamseh AMK, Vet B, Šutta P, Zeman M. Modeling and optimization of a-Si:H solar cells with ZnO: Al back reflector. *Solar Energy Materials and Solar Cells* 2010; **94**(12): 2119–2123. DOI: 10.1016/j.solmat.2010.06.039
53. Pieters BE, Stiebig H, Zeman M, van Swaaij RACMM. Determination of the mobility gap of intrinsic $\mu\text{c-Si:H}$ in *p-i-n* solar cells. *Journal of Applied Physics* 2009; **105**: 044502. DOI: 10.1063/1.3078044
54. Ulbrich C, Kirchartz T, Ding K, Pieters BE, Gerber A, Rau U. Spectrally dependent optimization of multi-junction solar cells, *Proceedings of the 24th European Photovoltaic Solar Energy Conference*: Hamburg, Germany, 2009; 2386–2389. DOI: 10.4229/24thEUPVSEC2009-3CO.12.3
55. Ferry VE, Verschuuren MA, Li HBT, Verhagen E, Walters RJ, Schropp REI, Atwater HA, Polman A. Light trapping in ultrathin plasmonic solar cells. *Optics Express* 2010; **18**(2): A237–A245. DOI: 10.1364/OE.18.00A237
56. Pflaum C, Haase C, Stiebig H, Jandl C. Simulation of light in-coupling at oblique angles in thin-film silicon solar cells, *Proceedings of the 24th European Photovoltaic Solar Energy Conference*: Hamburg, Germany, 2009. DOI: 10.4229/24thEUPVSEC2009-3BO.9.6
57. Jandl C, Hertel K, Pflaum C, Stiebig H. Simulation of silicon thin-film solar cells for oblique incident waves, *Proc. SPIE* 8065, 806505 2011. DOI: 10.1117/12.882860
58. Čampa A, Krč J, Topič M. Analysis and optimisation of microcrystalline silicon solar cells with periodic sinusoidal textured interfaces by two-dimensional optical simulations. *Journal of Applied Physics* 2009; **105**: 083107. DOI: 10.1063/1.3115408